Dominant effect of anharmonicity on the equation of state and thermal conductivity of MgO under extreme conditions

Choah Kwon [1], Yi Xia [2], Fei Zhou [3,*], and Byungchan Han [1,†]

[1] *Department of Chemical & Biomolecular Engineering, Yonsei University, 50 Yonsei-ro 03722, Seodaemun-gu, Seoul, Republic of Korea*
[2] *Department of Materials Science and Engineering, Northwestern University, Evanston, Illinois 60208, USA*
[3] *Physical and Life Sciences Directorate, Lawrence Livermore National Laboratory, Livermore, California 94550, USA*

Understanding heat transfer in the earth mantle region is of great scientific interest but highly challenging due to dissimilar conditions from our daily lives. Thermal conductivity of highly pressured and thermally activated materials can be completely different from that at ambient condition. In this study we calculate the equation of state and thermal conductivity of cubic crystalline MgO, a major component of the mantle, in such an environment. It is shown that the material properties are not accurately captured unless rigorous treatment of anharmonicity of phonon vibrational motion is explicitly applied. To predict renormalized phonon dispersion relations, interatomic force constants of high-order expansion are required, especially at elevated temperature. The anharmonicity plays an increasingly substantial role for regulating volume expansion as temperature rises, because the Gibbs free energy of MgO considerably deviates from what was predicted by the quasiharmonic approximation. We find that the lattice thermal conductivity of MgO and the heat transfer of the earth's mantle are reliably estimated only when both the temperature-dependent renormalization of phonon frequencies and four-phonon scattering effects are taken into consideration. We map the characteristics at Geotherm into contour diagrams in which equilibrium volumes and the thermal conductivities are described as functions of temperature and pressure. The thermal conductivity values of MgO in this study are smaller than those in previous theoretical studies due to the additional incorporation of four-phonon scatterings in the calculations. Specifically, deviation between the values in previous studies and in this study becomes larger as thermodynamic variables reach those near the core-mantle boundary. For instance, thermal conductivities of 52.15 and 23.67 $Wm^{-1} K^{-1}$ are estimated at ambient and extreme conditions ($T = 4000$ K and $P = 135$ GPa), respectively.

I. INTRODUCTION

Discovering the heat transfer in the earth mantle and at the core-mantle boundary (CMB) is a highly interesting while challenging problem due to significantly different thermodynamics from ambient conditions. In accordance with viscosity and phases of component materials, the mantle is divided into three territories: the upper and lower parts, and the transition zone in between them. The upper mantle mainly consists of ringwoodite phase which transforms into periclase and bridgmanite at the lower mantle [1–3]. Not only the multiphase nature of the mantle but also harsh thermodynamic conditions render accurate evaluation of its thermal conductivity (TC) challenging.

Enormous efforts have been pursed to predict the TC of MgO, since it is a common material of the lower mantle and often serves as a major component of the mantle [4,5]. Experimentally, several papers measured TCs of MgO not only at standard state, which are 49.9 $Wm^{-1} K^{-1}$ [6] and 53.00 $Wm^{-1} K^{-1}$ [7], but also at high pressure and temperature conditions. For instance, TCs of MgO at constant pressures of 8 and 14 GPa [8] were measured up to 1400 K.

Additionally, TCs of MgO at constant temperatures of 300 and 2000 K were measured until the pressure reaches up to 60 GPa [7]. However, these limited experimental conditions are not enough to exactly capture heat transfer in the deep mantle. TCs of MgO were also theoretically estimated using first-principles molecular dynamics (FPMD) [9–11] and density functional theory (DFT) calculations [12–16]. Several studies utilized equilibrium and nonequilibrium molecular dynamics to track the atomic movements and calculated TCs of MgO under various conditions. de Koker [9] calculated TCs of single-crystalline MgO at one volume ($V = 10.998 \, cm^3 \, mol^{-1}$) with varying temperature by applying FPMD to the kinetic conductivity relation. Stackhouse *et al.* [10] directly imposed the temperature gradient by using first-principles calculations with nonequilibrium molecular dynamics to predict TCs of MgO as functions of density and temperature. The study suggested TC at CMB as 20 $Wm^{-1} K^{-1}$ with ± 5 $Wm^{-1} K^{-1}$ uncertainty. Haigis *et al.* [11] made use of molecular dynamics with advanced ionic potential and the Green-Kubo relation to calculate TCs of MgO near CMB conditions of $T = 3000$ K and $P = 138$ GPa, which was 76.8 ± 4.4 $Wm^{-1} K^{-1}$.

On the other hand, TCs of MgO were predicted by solving the Boltzmann transport equation (BTE) with force constants obtained via DFT calculations. Tang *et al.* [12,13] investigated TCs of the mantle, which are in the range of 15 and
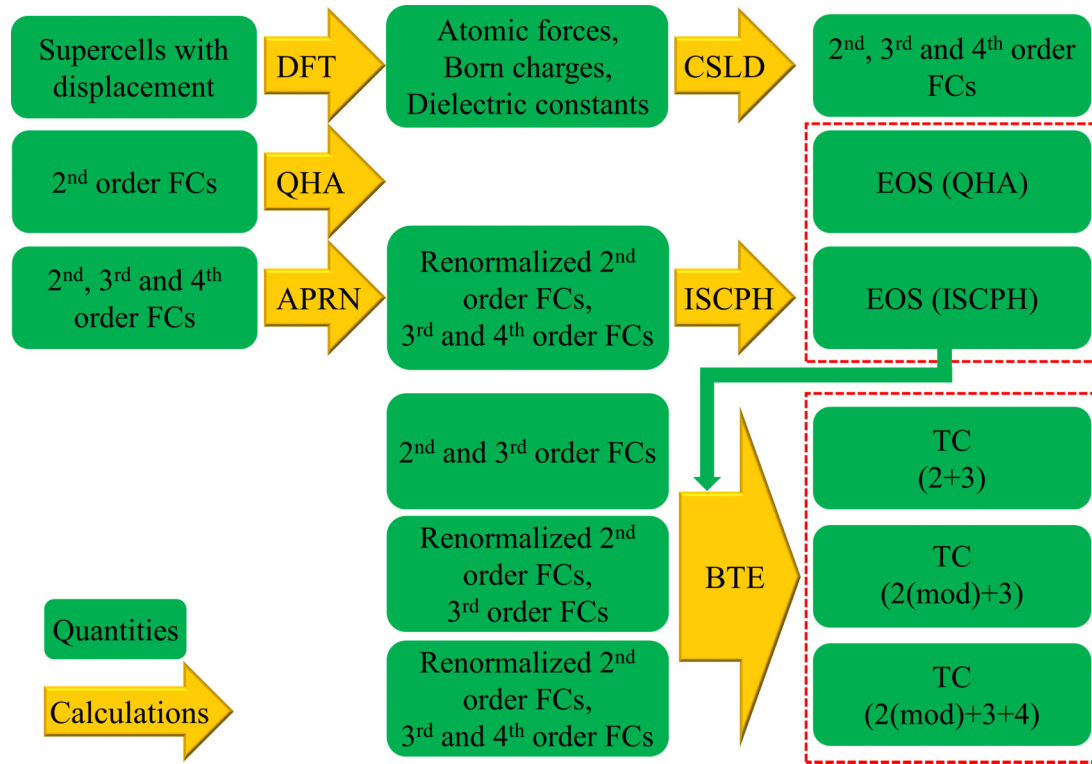
FIG. 1. Flow chart to obtain EOS and TC for MgO in red dotted boxes. The contents in green boxes indicate obtained quantities by calculation methods in yellow arrows. Abbreviations of force constant and thermal conductivity are expressed as FC and TC. Various computational methods are described in detail in Sec. II.

50 Wm^{-1} K^{-1}, by considering isotope and three-phonon scatterings in single-mode time approximation (SMTA) [12] and the relaxation time approximation (RTA) [13]. Dekura and Tsuchiya [14] took further steps to solve the BTE iteratively to get the full solution beyond the RTA. TCs of the full iterative solution are larger than those of RTA, and the two become closer as conditions of temperature and pressure reach to that of the mantle. For example, the TCs of full solution and RTA are calculated to be 53.7 and 42.2 Wm^{-1} K^{-1} at the standard state but are reduced to 39.7 and 31.6 Wm^{-1} K^{-1} at CMB. All these works considered three-phonon scattering mechanisms, which are the lowest rung in the perturbative treatment of interacting phonons. Four-phonon scatterings are expected to be increasingly important at high temperature but are considerably more challenging computationally [17]. A recent study by Puligheddu *et al.* [15] implemented four-phonon scattering in their calculations for MgO at a few selected conditions of 500, 750, and 1000 K at atmospheric pressure, predicting TCs of 32.8, 20.2, and 14.4 Wm^{-1} K^{-1}, respectively. Ravichandran and Broido [16] also calculated TCs of MgO, including four-phonon scattering at a constant temperature of 300 K with various pressure conditions up to 60 GPa, where the TC increases from 50 to 200 Wm^{-1} K^{-1}.

In spite of the large body of theoretical studies on TC of rocksalt MgO, we found that there are still ambiguous points in terms of accuracy of the TCs at extreme conditions. Specifically, this work is distinguished in two aspects compared to the previous works. First, a precise equation of state (EOS) for MgO was calculated at Geotherm because density significantly affects interatomic force constants. Previous papers on

TC calculations [12–14] did not pay much attention to EOS for MgO and referred the density from other papers. In this paper we obtained the temperature-dependent renormalized phonon spectra as well as EOS with explicit treatment of anharmonic vibrational contributions of phonons. We found excellent agreement of the equilibrium volume with experiments. Second, some papers [15,16] considered four-phonon scatterings in the calculations of TC for MgO, but the most extreme thermodynamic conditions of MgO considered were 300 K and 60 GPa, which is not relevant to heat transfer in the earth's mantle. In this work, TCs of MgO over wider ranges of temperatures and pressure values were calculated using the EOS, phonon renormalization, and four-phonon processes that are expected at elevated temperature. Our work, therefore, provides truly *ab initio* predictions on the thermodynamics and thermal transport properties of cubic MgO.

II. COMPUTATIONAL METHOD

A brief explanation of our computational approach is as follows (Fig. 1). The equilibrium volumes of MgO with varying thermodynamic conditions were first evaluated by the quasiharmonic approximation (QHA). Since it was well known that the QHA ignores the explicit anharmonic contribution to the vibrational free energy at constant volume, we were able to improve EOS predictions with the more sophisticated anharmonic phonon renormalization (APRN) process at finite temperature [18] and improved self-consistent phonon (ISCPH) theory [19], which employs the interatomic force constants of MgO up to fourth order to compute the renormal-

ized phonon spectra and vibrational free energy to predict the EOS of MgO. The approach of volume prediction by ISCPH is consistent with Ref. [19]. Then the TC of MgO was calculated at three different approximation levels: (i) three-phonon scattering with harmonic phonon spectra, or 2+3, which is computationally inexpensive but not expected to hold up well at extreme conditions, (ii) three-phonon scattering with renormalized phonon spectra, or 2(mod)+3 and (iii) three- and four-phonon scattering with renormalized phonons, or 2(mod)+3+4, an approach substantially more demanding to compute. To make a direct comparison between the different TC calculations, the same ISCPH predictions of equilibrium volume of MgO were adopted. Finally, we summarized the results by constructing contour maps of the equilibrium volumes (densities) and TCs of MgO with illustration. *Geotherm* as a prototype of mantle in the upper mantle, transition zone, lower mantle, and CMB regions. In this work the electronic TC was neglected, since MgO is a wide-band-gap insulator.

A. Density functional theory (DFT) and compressive sensing lattice dynamics (CSLD)

In accordance with a wide range of thermodynamic conditions, from ambient to the earth mantle states, the densities of rocksalt MgO ranging from 2.72 to $6.72\,\mathrm{g\,cm^{-3}}$ were modeled in 19 supercells of different lattice parameters in first-principles calculations (see Supplemental Material of Table SI [20]). The Vienna *ab initio* simulation package (VASP) [21] was utilized to obtain internal energy, forces, Born effective charges, and dielectric constant at each lattice constant in a primitive MgO cell. The internal energy and forces were calculated in $4 \times 4 \times 4$ conventional supercells of the rocksalt unit cell with varying atomic displacement of 0.01, 0.03, 0.06, 0.05, and 0.10 Å from the equilibrium positions, in accordance with previous calculations to facilitate calculation of harmonic and anharmonic force constants (FCs) [22,23]. Perdew-Burke-Ernzerhof (PBE) parametrization of the generalized gradient approximation (GGA) revised for solid (PBEsol), and Mg_sv and O_h of PAW potentials were applied in our calculations. Elastic constants and bulk modulus were calculated by applying different exchange-correlation functionals to select optimum exchange-correlation functionals as represented in Fig. S2 of the Supplemental Material [20]. Energy convergence and cutoff energy of the plane-wave basis set were chosen as 10^{-8} and 900 eV, respectively. The reciprocal space was sampled with $1 \times 1 \times 1$ and $9 \times 9 \times 9$ meshes for the supercell and primitive cell, respectively. In the case of Born effective charge and dielectric constant calculations, density functional perturbation theory (DFPT) [24,25] was utilized. Interatomic FCs of second, third, and fourth orders were extracted from the first-principles calculations using the compressive sensing lattice dynamics (CSLD) program [22,23,26]. To obtain phonon dispersion spectra, dynamical matrices were derived from second-order FCs [22]. In particular, the second-order terms were obtained by first subtracting the long-range dipole-dipole interactions analytically from initial FCs by CSLD, fitting the remaining short-range FCs, and finally, adding back the dipole terms to the dynamical matrices, therefore automatically accounting for the long-wavelength nonanalytic FCs [22]. To verify the reliability of

results from CSLD program, several tests which are to analyze root-mean-square error (RMSE) of forces by CSLD were conducted as inserted in Fig. S3 of the Supplemental Material [20]. Although RMSE gets larger at high temperature, as shown in Fig. S3b, the accuracy of the results from CSLD was validated in the prediction of TC for MgO when higher-order interatomic constants were participated. Convergence testing of third- and fourth-order interatomic FCs was conducted as a function of cutoff distance as represented in Figs. S4 and S5 of the Supplemental Material [20]. From the test, the converged cutoff distances of third- and fourth-order FCs are fifth nearest-neighbor (NN) and second NN, and those values were utilized to calculate EOS and thermal conductivity.

B. Quasiharmonic approximation (QHA)

The QHA is a widely used approximation for free-energy calculations of solids with harmonic oscillatory motions of phonons [27]. In this approach the thermodynamic equilibrium volume at given P and T is evaluated by minimizing the free energy with respect to volume as

$$F^{\mathrm{QHA}} = \min_{V} \left\{ E_0(V) + \frac{1}{N\beta} \sum_q \ln \left[2\sinh\left(\frac{1}{2}\beta\hbar\omega_q\right) \right] \right\}. \tag{1}$$

In Eq. (1), $E_0(V)$ represents the internal energy at volume of V and $T = 0$ calculated by first principles. The second term incorporates the zero-point energy and the vibrational free energy of phonons, while it should be noted that ω_q and β denote energy of phonon at q which is composed of reciprocal space and phonon mode and thermodynamic beta, respectively. In this work the electronic entropy was neglected due to a characteristic of MgO as a wide-band-gap insulator.

QHA is a simple but reasonably accurate method for predicting equilibrium volume at low temperature but shows significant deviation at high temperature due to its failure to fully capture the anharmonic effects in such conditions [28,29].

C. Anharmonic phonon renormalization (APRN) and improved self-consistent phonon (ISCPH) theory

The harmonic vibrational phonons with second-order FCs are valid, however, only for low temperature and are insufficient at extreme thermodynamic (high-temperature) conditions of the mantle. Therefore we utilized anharmonic phonon renormalization [18] with fourth-order FC expansion. To account for the APRN at finite temperature, we consider the first-order correction to the phonon frequency from quartic anharmonicity using self-consistent phonon theory [30–32]. The resulting self-consistent equation reads

$$\Omega_q^2 = \omega_q^2 + 2\Omega_q I_q, \tag{2}$$

where Ω_q is the renormalized harmonic phonon frequency for phonon mode q (a composite index for both wave vector and branch). The quantity I_q is defined as

$$I_q = \frac{\hbar}{8} \sum_{q'} \frac{V^{(4)}(q, -q, q', -q')}{\Omega_q \Omega_{q'}} \left[1 + 2n_{\Omega_{q'}}\right], \tag{3}$$

where n_X and $V^{(4)}$ are the phonon population with phonon energy of X and the reciprocal representation of the fourth-order interatomic FCs, respectively. As can be inferred from Eq. (3), the temperature effect is contained in the phonon population n. In practice, we solve Eqs. (2) and (3) in an iterative manner until Ω numerically converges.

With these renormalized phonon energies, the vibrational free energy from QHA is corrected by accounting for the contributions from quartic anharmonicity. The resulting vibrational free energy is denoted as $F_{\text{vib}}^{\text{SCPH}}$ and has the form

$$F_{\text{vib}}^{\text{SCPH}} = \frac{1}{\beta} \sum_q \ln\left[2 \sinh\left(\frac{1}{2}\beta\hbar\Omega_q\right)\right]$$
$$- \frac{\hbar}{8} \sum_q \left(\Omega_q - \frac{\omega_q^2}{\Omega_q}\right)[1 + 2n_{\Omega_q}], \quad (4)$$

where the first term has the same form as the QHA but with renormalized phonon energy and the rest are corrections from APRN as has been detailed in the literature [30]. It should be noted that $F_{\text{vib}}^{\text{SCPH}}$ still does not include the contribution from the odd-order anharmonic terms. An ISCPH theory has been proposed [19] to further account for the third-order anharmonicity. The associated vibrational free energy F_{vib}^{ISCPH} is

$$F_{\text{vib}}^{ISCPH} = F_{\text{vib}}^{\text{SCPH}} + F_{\text{vib}}^{\text{cubic}}, \quad (5)$$

$$F_{\text{vib}}^{\text{cubic}} = -\frac{\hbar^2}{48} \sum_{q_1,q_2,q_3} \frac{|V^{(3)}(q_1,q_2,q_3)|^2}{\Omega_{q_1}\Omega_{q_2}\Omega_{q_3}}$$
$$\times \left[\frac{\left(1 + n_{\Omega_{q_1}}\right)\left(1 + n_{\Omega_{q_2}} + n_{\Omega_{q_3}}\right) + n_{\Omega_{q_2}} n_{\Omega_{q_3}}}{\Omega_{q_1} + \Omega_{q_2} + \Omega_{q_3}}\right.$$
$$\left. + 3\frac{n_{\Omega_{q_1}} n_{\Omega_{q_2}} - n_{\Omega_{q_2}} n_{\Omega_{q_3}} + n_{\Omega_{q_3}} n_{\Omega_{q_1}} + n_{\Omega_{q_1}}}{-\Omega_{q_1} + \Omega_{q_2} + \Omega_{q_3}}\right]. \quad (6)$$

It is worth noting that the above formalism was recently employed by Oba *et al.* [33] to study the phonon anharmonicity and negative thermal expansion in ScF_3.

D. Equation of state (EOS)

EOS is acquired by integrating the introduced methods (Secs. II A–II C), as suggested in the first three rows of Fig. 1.

The prerequisite data, i.e., the Born effective charges, dielectric constant, and FCs, are calculated from DFT and CSLD to get the EOS for MgO. To obtain the free energy and the resulting EOS, two different methods for free energy F were used depending on whether anharmonic effects are explicitly contained or not. The method of QHA predicts volume without considering explicit anharmonicity and the vibrational free energy of phonon is derived only from second-order FCs. On the other hand, explicit anharmonicity up to the fourth order is introduced into the free energy F by using APRN and IS-CPH methods. F is first corrected by APRN, which generates modified second-order FCs and shifted phonon frequencies from fourth-order FCs according to Eqs. (2)–(4). Then another improvement to F by ISCPH inserts correction from the third-order FC, according to Eqs. (5) and (6).

E. Thermal conductivity (TC)

In this work we ignore the electronic contribution to TC as MgO is a wide-band-gap insulator. Lattice TC can be evaluated by solving BTE [34], which is shown in Eq. (7):

$$\kappa_{\alpha\beta} = \frac{\beta}{T\sigma N} \sum_q n_{\omega_q}(n_{\omega_q} + 1)(\hbar\omega_q)^2 v_\alpha \otimes v_\beta \tau_q. \quad (7)$$

Here $\kappa_{\alpha\beta}$ represents components of the tensor matrix for TC. The index q denotes both modes of phonon and reciprocal coordinates. For a given q, the energy of the phonon and group velocity in the α direction are indicated by $\hbar\omega_q$ and v_α, respectively. The Bose-Einstein distribution at the energy of $\hbar\omega_q$ and the volume of the primitive cell are expressed by n_{ω_q} and σ, respectively. Relaxation time (τ_q), which is an inversion of scattering rate, means time until a scattering event. In this paper, isotope, three-phonon, and four-phonon scatterings, which conserve energy and momentum in the ways of N process and U process [27], were considered and connected by Matthiessen's rule [27]. The formulas of three- and four-phonon scattering rates at q are based on the single-mode relaxation time approximation (SMRTA) [17] and expressed in Eqs. (8) and (9), respectively:

$$\tau_{3\text{ph},q}^{-1} = \sum_{q_1 q_2}\left\{\frac{1}{2}\left(1 + n_{\omega_{q_1}} + n_{\omega_{q_2}}\right)\varsigma_- + \left(n_{\omega_{q_1}} - n_{\omega_{q_2}}\right)\varsigma_+\right\}, \quad (8)$$

$$\tau_{4\text{ph},q}^{-1} = \sum_{q_1 q_2 q_3}\left\{\frac{1}{6}\frac{n_{\omega_{q_1}} n_{\omega_{q_2}} n_{\omega_{q_3}}}{n_{\omega_q}}\varsigma_{--} + \frac{1}{2}\frac{\left(1 + n_{\omega_{q_1}}\right)n_{\omega_{q_2}} n_{\omega_{q_3}}}{n_{\omega_q}}\varsigma_{+-} + \frac{1}{2}\frac{\left(1 + n_{\omega_{q_1}}\right)\left(1 + n_{\omega_{q_2}}\right)n_{\omega_{q_3}}}{n_{\omega_q}}\varsigma_{++}\right\}, \quad (9)$$

with

$$\varsigma_\pm = \frac{\pi\hbar}{4N}|V^{(3)}(q, \pm q_1, -q_2)|^2 \delta(k \pm k_1 - k_2)\frac{\delta\left(\omega_q \pm \omega_{q_1} - \omega_{q_2}\right)}{\omega_q \omega_{q_1} \omega_{q_2}}, \quad (10)$$

$$\varsigma_{\pm\pm} = \frac{\pi\hbar^2}{8N^2}|V^{(4)}(q, \pm q_1, \pm q_2, -q_3)|^2 \delta(k \pm k_1 \pm k_2 - k_3)\frac{\delta\left(\omega_q \pm \omega_{q_1} \pm \omega_{q_2} - \omega_{q_3}\right)}{\omega_q \omega_{q_1} \omega_{q_2} \omega_{q_3}}, \quad (11)$$

where $V^{(3)}(q, \pm q_1, -q_2)$ and $V^{(4)}(q, \pm q_1, \pm q_2, -q_3)$ in Eqs. (10) and (11) are

$$V^{(3)}(q, \pm q_1, -q_2) = \sum_{b,l_1 b_1,l_2 b_2} \sum_{\alpha\alpha_1\alpha_2} \Phi^{(3)\alpha,\alpha_1,\alpha_2}_{0b,l_1 b_1,l_2 b_2} \frac{e^q_{\alpha b} e^{\pm q_1}_{\alpha_1 b_1} e^{-q_2}_{\alpha_2 b_2}}{\sqrt{m_b m_{b_1} m_{b_2}}} e^{\pm i k_1 \cdot r_{l_1}} e^{-i k_2 \cdot r_{l_2}}, \quad (12)$$

$$V^{(4)}(q, \pm q_1, \pm q_2, -q_3) = \sum_{b,l_1b_1,l_2b_2,l_3b_3} \sum_{\alpha\alpha_1\alpha_2\alpha_3} \Phi^{(4)\alpha,\alpha_1,\alpha_2,\alpha_3}_{0b,l_1b_1,l_2b_2,l_3b_3} \frac{e^q_{\alpha b} e^{\pm q_1}_{\alpha_1 b_1} e^{\pm q_2}_{\alpha_2 b_2} e^{-q_3}_{\alpha_3 b_3}}{\sqrt{m_b m_{b_1} m_{b_2} m_{b_3}}} e^{\pm ik_1 \cdot r_{l_1}} e^{\pm ik_2 \cdot r_{l_2}} e^{-ik_3 \cdot r_{l_3}}. \tag{13}$$

It is worth mentioning that the basis atom, primitive cell, Cartesian coordinate, and mass are denoted as b, l, α, and m, respectively. The polarization vector and wave vector of the phonon in Eqs. (10)–(13) are conveyed as e^q and k, respectively. The third- and fourth-order interatomic force constants in real space are $\Phi^{(3)\alpha,\alpha_1,\alpha_2}_{0b,l_1b_1,l_2b_2}$ and $\Phi^{(4)\alpha,\alpha_1,\alpha_2,\alpha_3}_{0b,l_1b_1,l_2b_2,l_3b_3}$, respectively. Due to the selection rule of phonon scattering, energy and momentum conservation are regulated by δ functions in Eqs. (10) and (11).

The three-phonon scattering is assorted into destruction (τ^{-1}_{3rd-m}) and creation (τ^{-1}_{3rd-p}) processes which are first and second terms of Eq. (8). On the other hand, the four-phonon scattering is further classified into three consequent processes on the aspect of rest phonons after the scattering: splitting (τ^{-1}_{4th-mm}), redistribution (τ^{-1}_{4th-pm}), and recombination (τ^{-1}_{4th-pp}) [35], which are the first, second, and third terms of Eq. (9), respectively. To calculate scattering rates of three-phonon scattering, an iterative method [36,37], which is beyond RTA, was adopted to correct underestimated thermal conductivity originated from the N process. But the RTA was utilized to gain rates of four-phonon scattering due to its complication and huge computational cost. We adopted this balanced method between accuracy and computational cost to obtain the thermal conductivity of MgO over a wide range of temperature and pressure condition. Other scattering channels, such as the resonance of three-phonon scattering [38] and higher-order phonon processes, are not considered in this work.

Based on the equilibrium volume predicted by ISCPH for a given thermodynamic condition, TC of MgO was calculated under three different classes of approximations, as they have been adopted in our earlier studies [18,39] with varying level of accuracy. As shown in the lower part of Fig. 1, the simplest one is 2+3 order expansion, which only considers the relaxation time for isotope and three-phonon scatterings. This is also the most commonly adopted method in the literature. The second approach is 2(mod)+3, which replaces bare phonon frequency with those shifted by APRN. One more step above on the ladder of theoretical sophistication is the 2(mod)+3+4 method, which further considers four-phonon scatterings according to the fourth-order FCs. A modified SHENGBTE program [18,36] incorporating these schemes was employed to obtain not only TCs of MgO in this section but also free energies in Secs. II B and II C. When calculating these properties from the program, FCs for a $5 \times 5 \times 5$ supercell of MgO and $15 \times 15 \times 15$ meshes of reciprocal space were set as inputs with dielectric constants and Born effect charges of corresponding volumes.

III. RESULTS AND DISCUSSION

EOS and TCs for MgO over a wide range of temperature and pressure conditions were obtained. We selected four pairs of (T, P) conditions: (300 K, 0.4 GPa), (300 K, 34.3 GPa), (2000 K, 2.7 GPa), and (2000 K, 34.4 GPa) in order to decouple the temperature and pressure effects on the EOS and TC of MgO. Section III consists of three sections: A. Phonon renormalization, B. Equilibrium volume, and C. Thermal conductivity. Alterations of phonon dispersion spectra by renormalization as functions of temperature and pressure are discussed in Sec. A because clarification of an anharmonic effect on phonon band structure is crucial to phonon-related properties. Predicted EOS and TC for MgO in terms of different methods and thermodynamic variables are analyzed in Secs. B and C, respectively.

A. Phonon renormalization

To illustrate the effects of phonon renormalization, we show in Fig. 2 the calculated phonon band structure predicted for four different volumes representing four combinations of thermodynamic conditions: low/high temperature (LT/HT) and low/high pressure (LP/HP). The quantitative correspondence between volume and T-P conditions, i.e., the EOS, is discussed in Sec. III B. For each fixed volume, the phonon dispersion curves (black solid lines) of Fig. 2 in the harmonic approximation were shown, which were directly derived from the second-order FCs and valid only in temperatures close to 0 at that volume, as well as renormalized phonons (red solid lines) according to the APRN by Eqs. (2) and (3). The latter are always higher in energy due to temperature-induced phonon hardening. The difference between the renormalized and harmonic phonon energies, or the amount of phonon hardening, varies depending on thermodynamic conditions. At LT (300 K), there is little difference between black solid (unrenormalized) and red solid (renormalized) lines in Figs. 2(a) and 2(b) in phonon band structure because the displacements of atoms are small enough to lie within the range of validity of the harmonic oscillation approximation. On the other hand, phonons at high temperature (2000 K) are severely hardened, as shown in Figs. 2(c) and 2(d), since the atomic displacements are so large that the harmonic expansion approximation becomes poor. The phonon hardening is especially pronounced under low pressure [Fig. 2(c)], as the density of states clearly elucidates anharmonicity effects showing that overall energies of phonons shift up. The phonons under high temperature and pressure conditions [Fig. 2(d)] are not hardened as much as those under high-temperature and low-pressure regions [Fig. 2(c)], since the atomic displacements are more restrained as mutual distances between atoms are shortened. From the results in Fig. 2, volume change and anharmonicity should be simultaneously contemplated to correctly describe phonon dispersion spectra.

B. Equilibrium volume

The equilibrium volumes were determined within the framework of QHA and ISCPH by minimizing free-energy
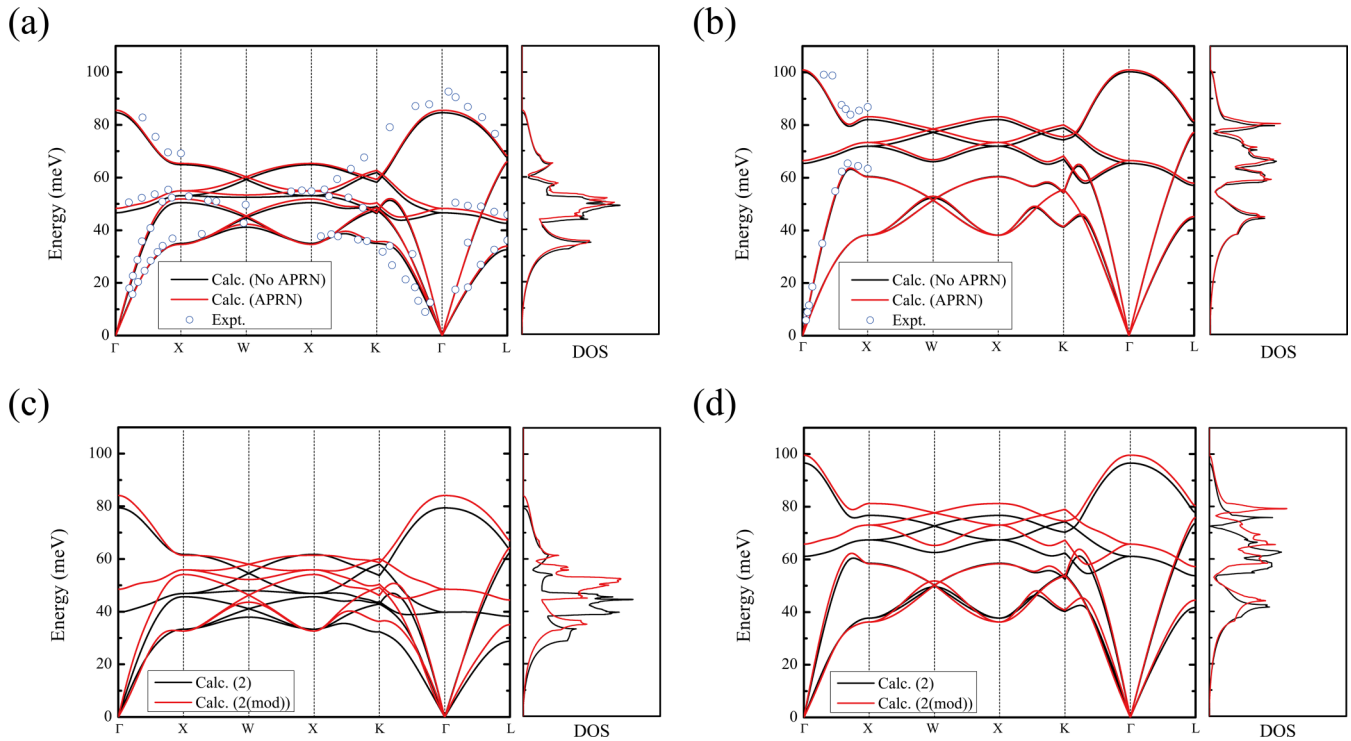
FIG. 2. Phonon dispersion spectra and density of states at (a) $T = 300$ K, $P = 0.4$ GPa, and $V = 19.02$ Å^3 (LT/LP); (b) $T = 300$ K, $P = 34.3$ GPa, and $V = 16.19$ Å^3 (LT/HP); (c) $T = 2000$ K, $P = 2.7$ GPa, and $V = 20.10$ Å^3 (HT/LP); and (d) $T = 2000$ K, $P = 34.4$ GPa, and $V = 16.81$ Å^3 (HT/HP). Both the harmonic and the renormalized phonon spectra at each given (T, P) condition were obtained at the same volume $V(T, P)$ as determined by the EOS from ISCPH (see also later discussions). The black (red) lines indicate phonon band spectra and density of states by second-order FCs (renormalized second-order FCs), which is expressed as 2 [2(mod)]. The phonon energies measured by neutron scatterings in (a) and (b) are cited from Refs. [45] and [46] and marked in blue open circles.

functionals as a function of volume for a given temperature and pressure, as exemplified in Fig. 3. It is clearly represented in Fig. 3 that the deviation between free energies by QHA and ISCPH is severe at high temperature. According to the results, the equilibrium volume by QHA very much disagrees with that by ISCPH at HT/LP regions as depicted in Fig. 4. At 0 GPa the equilibrium volumes predicted by QHA and ISCPH look rather similar up to 1000 K, as shown in Fig. 4(a). This is ascribed to the fact that the anharmonicity of the phonon at the condition is insignificant, as represented by differences of less than 1.14 meV/MgO between free energies by QHA and ISCPH at $T = 300$ K and $P = 0$ GPa [Fig. 3(a)]. The volume differences estimated by QHA and ISCPH at 0 GPa in Fig. 4(a) become severe as the temperature rises above about 1000 K, indicating that the energy profile of the phonons in MgO deviates from a harmonic oscillation approximation under those conditions. For instance, the equilibrium volumes of MgO at 964, 1973, and 2973 K [40] at atmospheric pressure were measured as 19.16 Å^3, 20.19 Å^3, and 21.42 Å^3, which continuously increase as temperature rises. The predicted volumes by QHA at the same conditions are 19.85 Å^3, 21.86 Å^3, and 32.50 Å^3, and those by ISCPH are 19.67 Å^3, 20.58 Å^3, and 21.57 Å^3, respectively. The equilibrium volumes of MgO by QHA and ISCPH both expand with ascent of temperature, but the volume of ISCPH is far more reliable, especially at higher temperatures than that of QHA. This can be attributed to exertion of anharmonicity on the free energy, as shown in Fig. 3. But the volumes of QHA and ISCPH at pressure

above 50 GPa show small difference, even at high temperature [Fig. 4(a)]. This is because the atomic displacement as well as anharmonicity effect are suppressed at such extremely high pressures, as represented in Figs. 3(c) and 3(d).

As shown in Figs. 4(a)–4(d), notably, the ISCPH method more accurately reproduces the MgO volume expansion than QHA. In Figs. 4(e) and 4(f), previously reported Geotherms for the mantle [41,42] are marked as square (upper mantle), star (transition zone), and circle (lower mantle). In QHA, the density of MgO slowly changes from 3.51 to 3.61 g cm^{-3} as the upper mantle goes to a deeper region. The density estimated by ISCPH shifts from 3.51 to 3.64 g cm^{-3} for the same condition. In the transition and lower mantle zones, the MgO density continuously increases and reaches 4.52 and 4.51 g cm^{-3} by QHA and ISCPH methods, respectively. At the CMB condition, which is 135 GPa and 4000 K, densities are predicted by QHA and ISCPH as 4.99 and 4.98 g cm^{-3}, respectively. Therefore the thermodynamic condition of the upper mantle is high temperature and relatively low pressure, which leads to deviation between volumes predicted by QHA and ISCPH. But the method of QHA well describes the volume near CMB conditions.

Based on the results of ISCPH, it is observed that the equilibrium volume expands as temperature rises via a phonon softening mechanism caused by higher vibrational entropy, but it shrinks as pressure increases due to the volumetric energy contribution in free energy. To quantify the dependency of volume on temperature and pressure, the thermal expansion
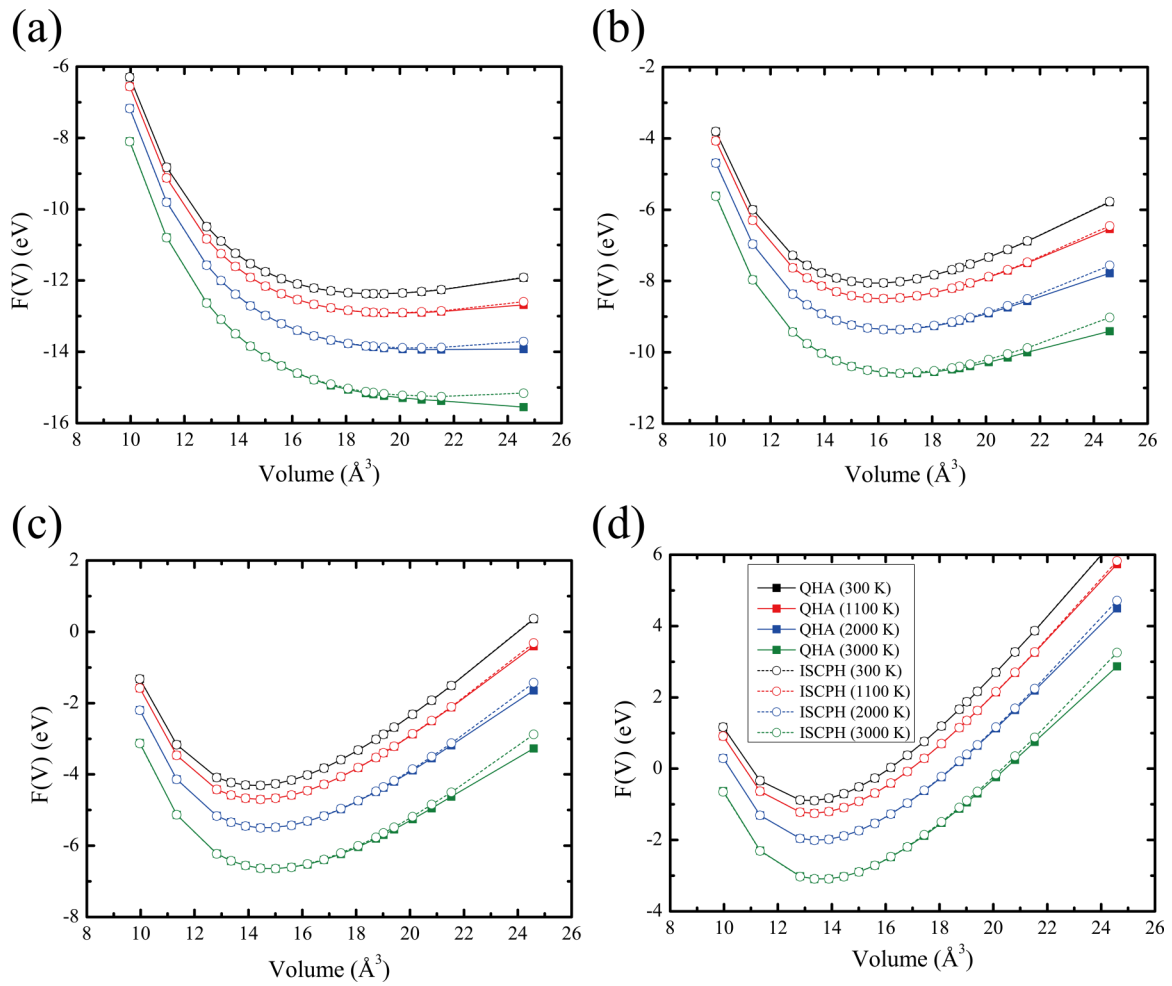
FIG. 3. Free energies, predicted by QHA and ISCPH in square and circle marks, as a function of volume at (a) 0, (b) 40, (c) 80, and (d) 120 GPa. The free energies in the figures at temperatures of 300, 1100, 2000, and 3000 K are expressed by black, red, blue, and green lines, respectively.

coefficients and bulk modulus of MgO were calculated by QHA and ISCPH, as shown in Fig. 5. It is clear that the ISCPH method more accurately predicts those properties than the QHA approach. For instance, thermal expansion coefficients by QHA and ISCPH at 1000 K and ambient pressure condition were calculated as $6.90 \times 10^{-5}\,\mathrm{K}^{-1}$ and $4.57 \times 10^{-5}\,\mathrm{K}^{-1}$, respectively [Fig. 5(a)], while the experimental measurement is $4.67 \times 10^{-5}\,\mathrm{K}^{-1}$ [43]. Figure 5(a) indicates that the thermal expansion coefficients at low pressures are higher than at high pressures. This originates from the fact that dependence of MgO volumes on temperature reduces as pressure increases.

The bulk modulus of MgO increases with pressure, meaning that to shrink the volume by the same amount, lower additional pressure is required at low pressure than at high pressure. The level of accuracy of QHA and ISCPH scrupulously appears at the prediction of bulk modulus. Compared to experimental data at 0 GPa, the predictive power of the QHA method is much worse than ISCPH at all conditions [Fig. 5(b)]. The bulk moduli shown in Fig. 5(b) were measured [44] as 160, 138, and 117 GPa at 300, 1100, and 1800 K, respectively, while remaining at ambient pressure, but bulk moduli of 146.0 and 147.7 GPa at 300 K, 108.9 and 126.8 GPa at 1100 K, and 53.3 and 108.1 GPa at 2000 K

under ambient pressure conditions as corresponding results of QHA and ISCPH, respectively. The bulk modulus by ISCPH well describes the measured value compared to that by QHA. These outcomes indicate that the QHA is not enough for an accurate description of the bulk moduli at such extreme thermodynamic conditions.

C. Thermal conductivity

1. Accuracy levels of three methodologies

TCs of MgO were calculated based on the equilibrium volume predicted by ISCPH under three different methodologies calculating the phonon dispersion relations and scattering rates as plotted in Fig. 6: 2+3, 2(mod)+3, and 2(mod)+3+4. To make a direct comparison between the different TC calculations, the same ISCPH predictions of equilibrium volume of MgO were adopted. Due to the phonon hardening mechanism, which increases the group velocity and decreases scattering rates of phonons, TCs from the 2+3 are smaller than those from 2(mod)+3. Changes of the three-phonon scattering rates with and without incorporation of the APRN were represented in Fig. 7 for four different conditions. The three-phonon scattering rates in Fig. 7 are results based on RTA to have
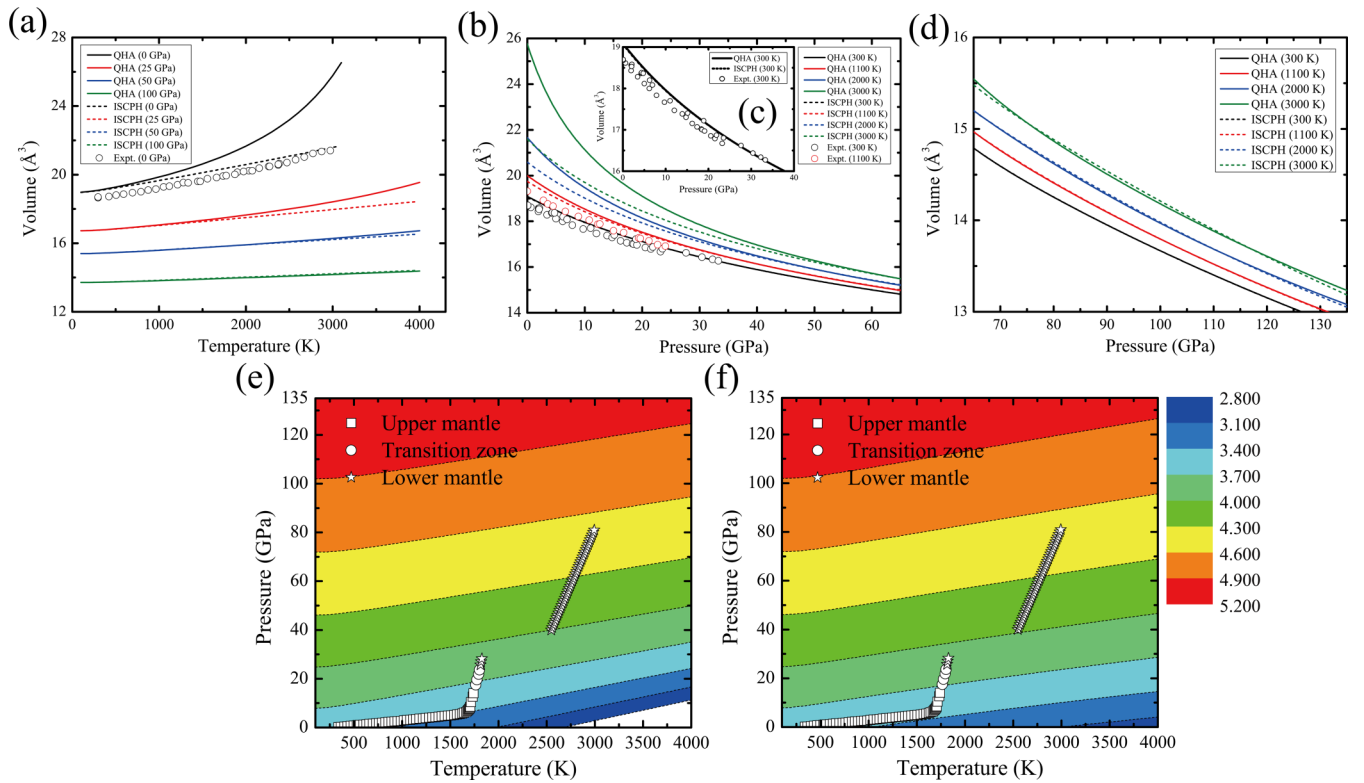
FIG. 4. Equilibrium volumes predicted via QHA and ISCPH (a) at constant pressures of 0, 50, 100, and 120 GPa and (b) at constant temperatures of 300, 1100, 2000, and 3000 K and (c) for low pressure (up to 65 GPa), and (d) for high-pressure regions. The equilibrium volumes at 300 K in (b) are separated in (c) to clearly show results. Contour maps of density with units of $g\,cm^{-1}$ predicted by (e) QHA and (f) ISCPH. The experimental values in (a) are referred from Refs. [40,47], and those in (b) and (c) are from [48]. The square, star, and circle marks in (e) and (f) denote Geotherms of the upper mantle, transition zone, and lower mantle from Refs. [41,42]. For given temperature and pressure, we used the same lattice constants as determined by the ISCPH equation of state, similar to Fig. 2.

consistency with the four-phonon scattering rates in Fig. 8. The scattering rates by the iterative method are similar to those by RTA, because the scattering of MgO is rather governed by U process than N process.

Since phonon hardening is more intensive at HT/LP conditions, the scattering rates evaluated by the 2(mod)+3 approach at this condition are grossly lowered as shown

in Fig. 7(c). The 2(mod)+3+4 method always predicts smaller TC than 2(mod)+3 due to the additional four-phonon scattering channels. Therefore, compared to 2+3, the two correctional mechanisms for TC prediction, phonon renormalization, and four-phonon scattering are counteractive. The impact of four-phonon scatterings on the TC is stronger at HT/LP conditions than at LT/HP conditions, as clearly shown
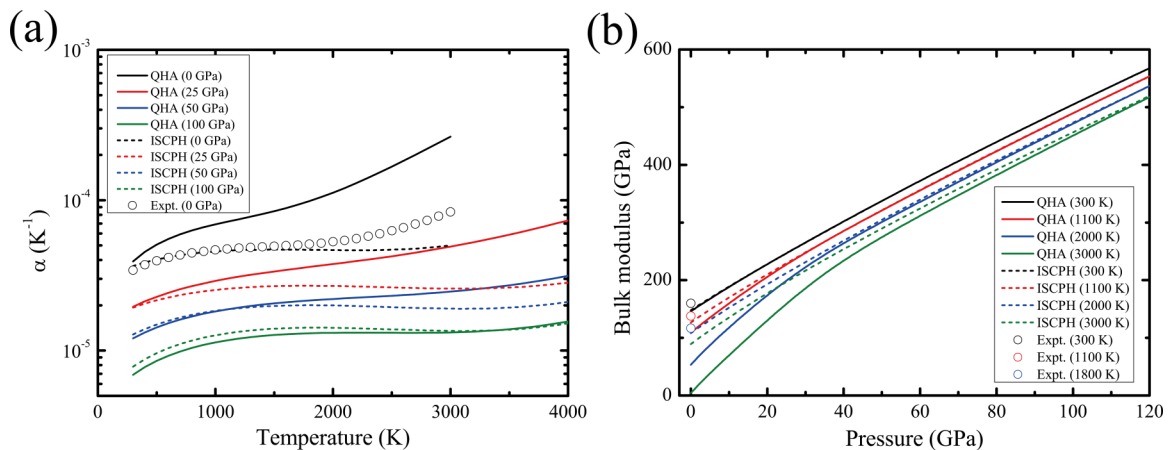

FIG. 5. (a) Thermal expansion coefficients of MgO as functions of temperature at 0, 25, 50, and 100 GPa. (b) Bulk moduli as functions of pressure at 300, 1100, 2000, and 3000 K. Solid and dotted lines represent results predicted by QHA and ISCPH, respectively. The experimental values are from Ref. [43] in (a) and from Ref. [44] in (b).
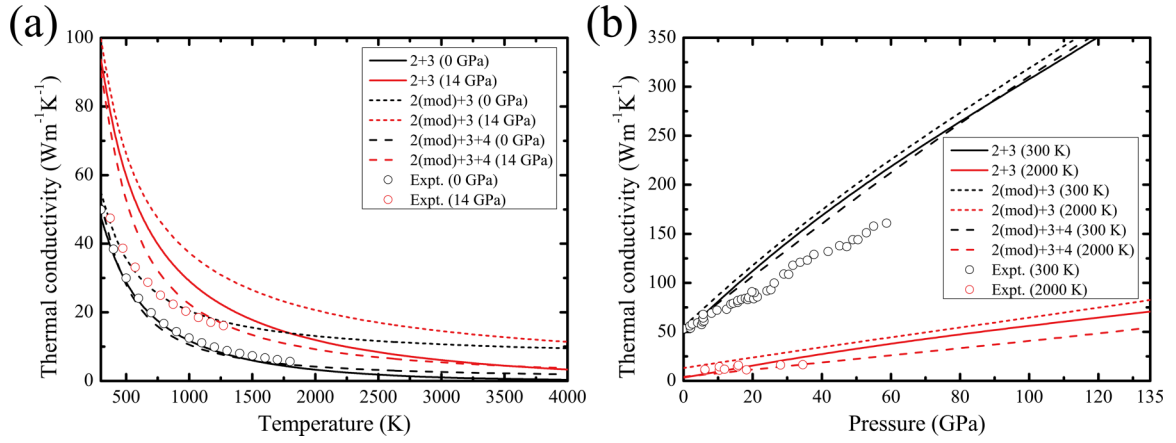
FIG. 6. (a) TCs as a function of temperature at $P = 0\,\text{GPa}$ and $P = 14\,\text{GPa}$. (b) TCs as a function of pressure at $T = 300\,\text{K}$ and $T = 2000\,\text{K}$. TCs obtained using 2+3, 2(mod)+3, and 2(mod)+3+4 are expressed in solid, short dashed, and dashed lines, respectively. The TCs measured by experiments at 0 and 14 GPa in Fig. 6(a) are obtained by Refs. [6,8,49] and those at 300 and 2000 K in Fig. 6(b) are gained by Ref. [7].

at Figs. 8(c) and 8(d). At the CMB, most of the scattering rates is distributed in the range of $10^{-6}\,\text{ps}^{-1}$ and $10^{1}\,\text{ps}^{-1}$. Although the temperature of CMB is extreme, the scattering process of phonons is restricted due to pressurized condition.

The calculated TC is generally larger than what was experimentally measured and is ascribed to several neglected factors in our study, such as defects and sizes of grains. These additional factors are more influential at high pressure. Previous research found that thermal conductivity of MgO is significantly affected by defects [16]. The calculated thermal conductivity of MgO at high pressure well matches

measured thermal conductivity of MgO compared to that of pristine MgO. Among the TC of the three different approaches (Fig. 6), the agreement between the 2(mod)+3+4 method and the experimental measurement is the best. One surprising observation is that TC by the 2+3 mechanism, which neither accounts for APRN nor four-phonon scatterings, seems better than the 2(mod)+3 approach. This is likely due to a cancellation of errors arising from the countervailing effects of APRN and four-phonon scatterings, in line with a recent study on PbTe [18]. This clearly indicates that anharmonicity and higher-order scattering rates of phonons should be simul-
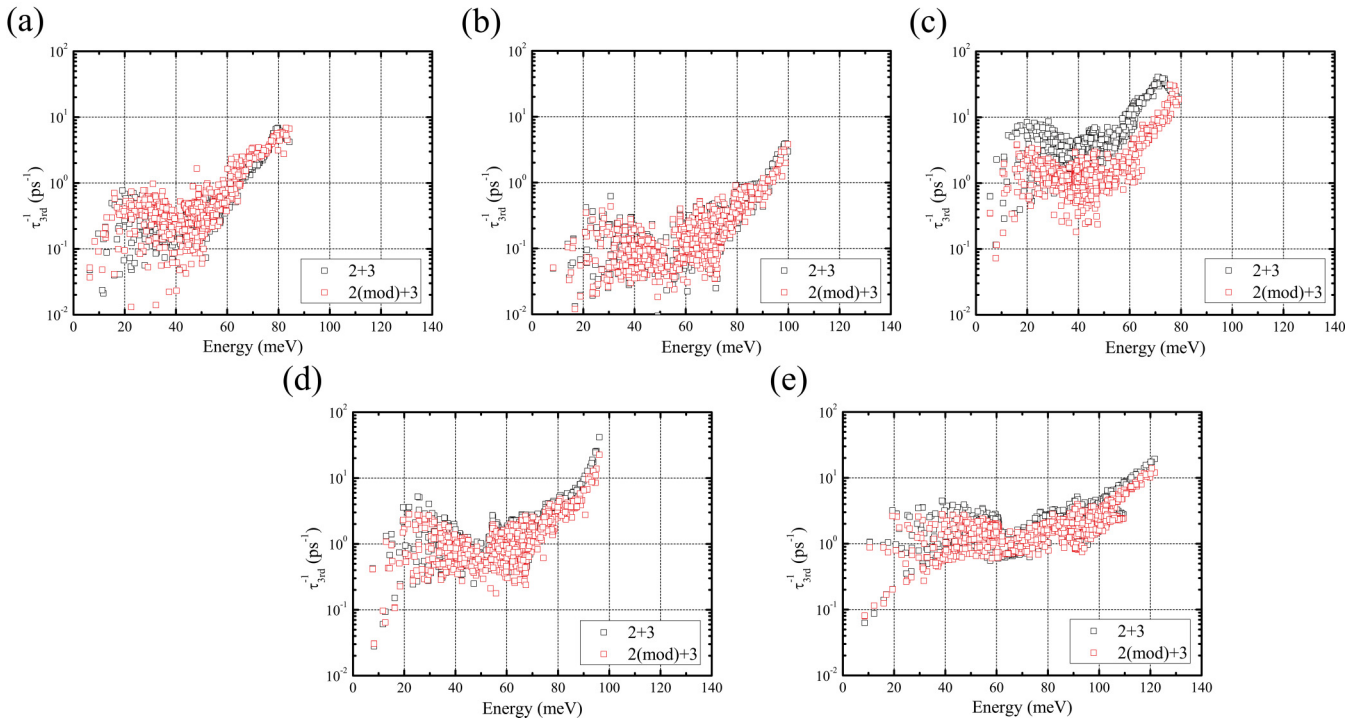

FIG. 7. Total three-phonon scattering rates based on RTA at (a) $T = 300\,\text{K}$ and $P = 0.4\,\text{GPa}$ (LT/LP), (b) $T = 300\,\text{K}$ and $P = 34.3\,\text{GPa}$ (LT/HP), (c) $T = 2000\,\text{K}$ and $P = 2.7\,\text{GPa}$ (HT/LP), (d) $T = 2000\,\text{K}$ and $P = 34.4\,\text{GPa}$ (HT/HP), and (e) $T = 4000\,\text{K}$ and $P = 139.2\,\text{GPa}$ (CMB). The black and red squares denote three-phonon scattering rates without and with considering APRN, respectively.
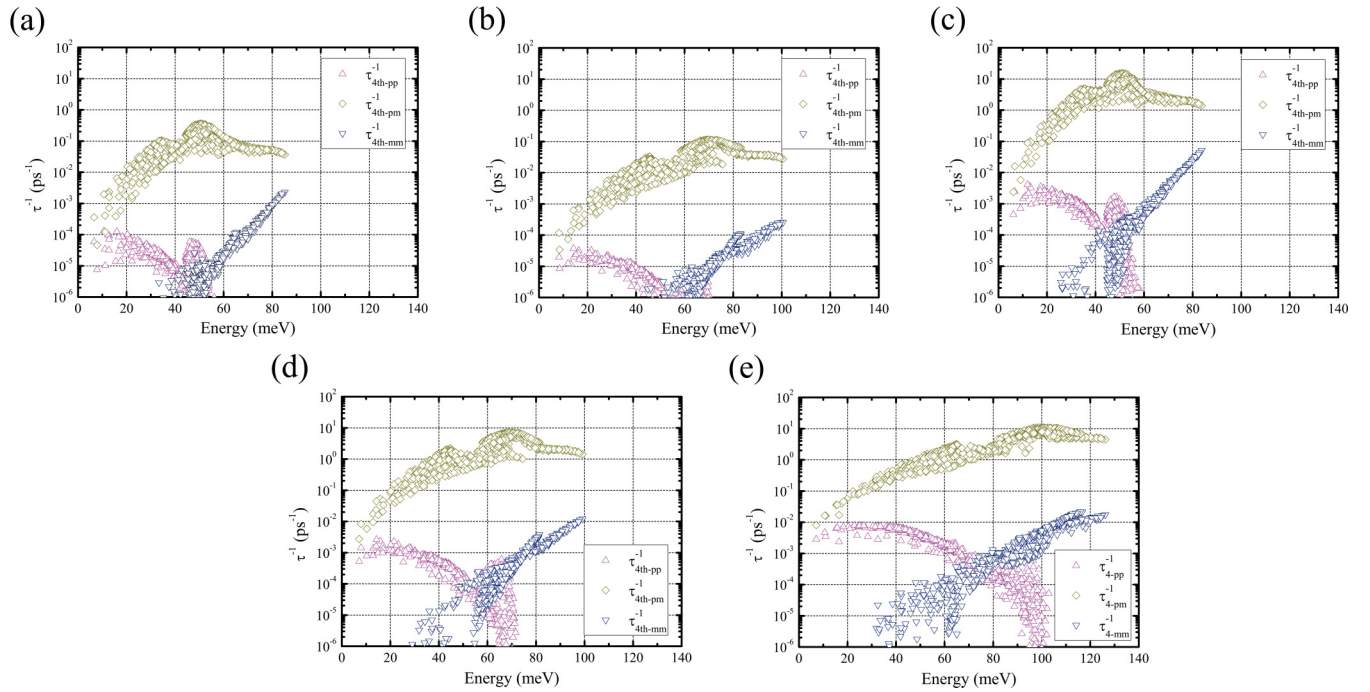
FIG. 8. Four-phonon scattering rates in the RTA at (a) $T = 300$ K and $P = 0.4$ GPa (LT/LP), (b) $T = 300$ K and $P = 34.3$ GPa (LT/HP), (c) $T = 2000$ K and $P = 2.7$ GPa (HT/LP), (d) $T = 2000$ K and $P = 34.4$ GPa (HT/HP), and (e) $T = 4000$ K and $P = 139.2$ GPa (CMB). Four-phonon scattering rates for splitting, redistribution, and combination processes are represented by navy inverted triangle, olive diamond, and magenta triangle, respectively.

taneously considered to get an accurate TC of MgO. This highlights the importance of carefully considering different physical mechanisms in TC calculations and suggests that coincidental cancellation of errors contributed to the previous success of the prevailing, relatively simple approach 2+3 in describing the TC of MgO.

2. Effect of temperature and pressure

At constant pressure the TC of MgO decreases as temperature increases, as shown in Fig. 6(a), which is a general trend for insulators. As temperature rises, the phonon softening reduces the group velocity but increases the scattering rate, which eventually decreases the TC. The four-phonon

scattering plays a key role for controlling the scattering rate in that it decreases TC at high temperature. In this way, the four-phonon scattering is one of the key factors that reduce TC at high temperature, as shown in Fig. 8. For example, Fig. 8 shows that the four-phonon scattering rates at HT/LP in Fig. 8(c) in the energy range of 40–60 meV are about 100 times larger than those at LT/LP in Fig. 8(a), while the scattering rates of three phonons under the same conditions at LT/LP in Fig. 7(a) are only about 10 times those in Fig. 7(c) at HT/LP.

Our calculations indicate that TC of MgO is linearly proportional to the pressure for a given temperature, as shown in Fig. 6(b). It is because the energy and group velocity of phonons increase, which reduces the scattering rates, as the
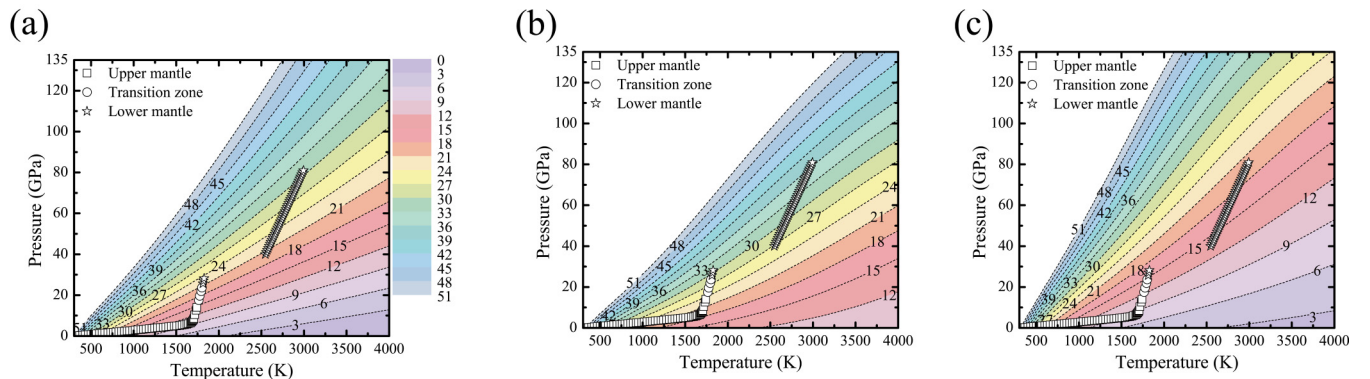

FIG. 9. Contour maps of TC for MgO, the unit of which is $Wm^{-1} K^{-1}$, of (a) 2+3, (b) 2(mod)+3, and (c) 2(mod)+3+4 mechanisms as functions of temperature and pressure. Geotherms of the upper mantle, transition zone, and lower mantle are cited from Refs. [41,42] and expressed by square, star, and circle marks.

TABLE I. The lowest and highest TCs of MgO in the upper and lower mantles and transition zone for 2+3, 2(mod)+3, and 2(mod)+3+4 levels. Unit of the TC is $Wm^{-1} K^{-1}$.

	2+3	2(mod)+3	2(mod)+3+4
Upper mantle	14.59–43.14	23.30–49.91	11.07–45.88
Transition zone	16.76–20.48	25.19–28.44	12.38–14.66
Lower mantle	21.58–30.79	29.41–36.66	15.35–19.89
CMB	34.05	43.49	23.67

MgO lattices are more pressurized. The linear dependency of the TC on pressure changes with temperature. For example, the linear slope of 2(mod)+3+4 in Fig. 6(b) changes from 2.50 at 300 K to 0.37 at 2000 K, which can be explained by thermal effects, such as frequent scattering and softening phonon dispersion, leading to a reduction of the TC.

In summary, the TC of MgO is approximately (inversely) proportional to pressure (temperature). This implies that as both temperature and pressure simultaneously increase, TC may not change significantly due to the counterbalance of the two conflicting effects. Then the ratio of temperature and pressure change should be a better descriptor for understanding TC and heat transfer of MgO. Figure 9 represents contour maps of the TC evaluated with 2+3, 2(mod)+3, and 2(mod)+3+4 formalisms. The TCs in three different zones are included in Table I. For the upper mantle, they change from the top to the bottom of the region: from 43.14 to 14.59 $Wm^{-1} K^{-1}$, from 49.91 to 23.30 $Wm^{-1} K^{-1}$, and from 45.88 to 11.07 $Wm^{-1} K^{-1}$ for the 2+3, 2(mod)+3,

and 2(mod)+3+4 methodology. In the case of the lower mantle, the trend of the variation is opposite to the upper mantle, which increases TCs of MgO to 30.79, 36.66, and 19.89 $Wm^{-1} K^{-1}$ of 2+3, 2(mod)+3, and 2(mod)+3+4 at the bottom of the lower mantle. The TCs of 2+3, 2(mod)+3, and 2(mod)+3+4 at CMB are 34.05, 43.49, and 23.67 $Wm^{-1} K^{-1}$, respectively, which has the same trend of the lower mantle, and the large amount of heat could be transferred in CMB compared to the lower mantle.

There are several previous studies [10,11,13,14] that predicted TCs of MgO under the conditions of the mantle, which are summarized in Table II. For example, TC of MgO at $T = 4100$ K and $P = 136$ GPa was calculated as 20 ± 5 $Wm^{-1} K^{-1}$ via nonequilibrium molecular dynamics simulations, but we obtained TC of 33.3, 42.8, and 23.2 $Wm^{-1} K^{-1}$ for the 2+3, 2(mod)+3, and 2(mod)+3+4 mechanism under the same thermodynamic conditions. The TC of 2(mod)+3+4 is most comparable to previous study among thermal conductivities of three mechanisms. Another study [11] based on molecular dynamics also calculated TC of 76.8 ± 4.4 $Wm^{-1} K^{-1}$ at $T = 3000$ K and $P = 138$ GPa, which is a much larger value than this work attributed by a different force field. The thermal conductivities of 2+3, 2(mod)+3, and 2(mod)+3+4 under these conditions are 47.3, 58.0, and 34.6 $Wm^{-1} K^{-1}$. There are several studies to understand heat transfer of MgO under extreme conditions based on first-principles calculations with solving the Boltzmann transport equation. The results of the studies are similar to those of 2+3 and 2(mod)+3 in this work. The thermal conductivities of MgO at the conditions of $T = 2800$ K, $P = 95$ GPa and T, $P = 2000$ K, $P = 100$ GPa were calculated as 40.07 $Wm^{-1} K^{-1}$

TABLE II. Thermal conductivities of MgO at various thermodynamic conditions with different methodologies. MD = molecular dynamics, NEMD = nonequilibrium MD, BTE = Boltzmann transport equation.

Thermal conductivity ($Wm^{-1} K^{-1}$)	Condition	Method	Reference
47.7/55.0/52.2		2+3/2(mod)+3/2(mod)+3+4	This work
111 ± 16		Classic MD	[11]
76	Ambient condition	BTE	[13]
53.7/42.2		BTE full/RTA	[14]
43.0/51.1		3+4-phonon (Unrenormalized/renormalized)	[16]
28.4/35.3/27.6	500 K,	2+3/2(mod)+3/2(mod)+3+4	This work
32.8	0 GPa	BTE-ALD	[15]
3.9/13.6/4.5	2000 K,	2+3/2(mod)+3/2(mod)+3+4	This work
5.9 ± 0.9	1 GPa	DFT NEMD	[10]
76.3/90.1/60.4	2000 K,	2+3/2(mod)+3/2(mod)+3+4	This work
42 ± 25	149 GPa	DFT NEMD	[10]
56.2/64.5/40.7	2000 K,	2+3/2(mod)+3/2(mod)+3+4	This work
60 ± 8	100 GPa	BTE full	[14]
37.8/44.7/25.3	2800 K,	2+3/2(mod)+3/2(mod)+3+4	This work
40.1	95 GPa	BTE	[13]
47.3/58.0/34.6	3000 K,	2+3/2(mod)+3/2(mod)+3+4	This work
76.8 ± 4.4	138 GPa	Classic MD	[11]
33.3/42.8/23.2	4100 K,	2+3/2(mod)+3/2(mod)+3+4	This work
20 ± 5	136 GPa	DFT NEMD	[10]
36.2/45.9/25.5	3800 K,	2+3/2(mod)+3/2(mod)+3+4	This work
39.7/35.0	136 GPa	BTE full/RTA	[14]

[13] and $60 \pm 8 \, \text{Wm}^{-1} \, \text{K}^{-1}$ [14], respectively. The thermal conductivities of 2+3, 2(mod)+3, and 2(mod)+3+4 were speculated as 37, 44.7, and 25.3 $\text{Wm}^{-1} \, \text{K}^{-1}$ at $T = 2800 \, \text{K}$ and $P = 95 \, \text{GPa}$ and 56.2, 64.5, and 40.7 $\text{Wm}^{-1} \, \text{K}^{-1}$ at $T = 2000 \, \text{K}$ and $P = 100 \, \text{GPa}$. From the comparison, it can be emphasized that four-phonon scattering significantly reduces the TC of MgO, meaning it is one of the pivotal factors to predict the TC of MgO under extreme conditions.

IV. CONCLUSIONS

We have calculated the EOS and lattice TC of MgO under a wide range of temperatures and pressures to understand heat transfer of the earth's mantle. The EOS for MgO was predicted by QHA as well as ISCPH to explicitly consider anharmonicity. It was confirmed that the thermodynamic equilibrium volume predicted by QHA at high temperature diverges and does not agree with experimental values, while that by ISCPH corrects QHA errors by incorporating anharmonic phonon vibrational motion explicitly in the vibrational free energy. Therefore it is crucial to contemplate anharmonicity to predict the volume of MgO at high temperatures. At high pressure, the errors of QHA are substantially less pronounced due to suppressed thermal displacement. Based on the volume of MgO predicted by ISCPH, it was confirmed that as temperature and pressure are further removed from the ambient condition, the thermal expansion coefficient and bulk modulus of MgO vary substantially. The thermal expansion coefficient of MgO gets smaller as external pressure increases, and bulk modulus becomes smaller as temperature rises. TCs of MgO were calculated under three different mechanisms— 2+3, 2(mod)+3, and 2(mod)+3+4. Our results indicate that not only phonon renormalization but also relaxation time, including effects of higher (fourth) order scatterings, are

essential to determine accurate TC, while uncontrolled cancellation of error was found in the prevailing 2+3 method (three-phonon scattering only of harmonic phonons). Due to phonon softening and frequent scatterings at high temperature, it is more difficult for MgO to transfer heat, while the opposite happens at high pressure. We conclude that accurate and quantitative consideration of the combined effects are necessary. For the application to mantle, the equilibrium volume predicted by ISCPH varies from 3.51 to 4.98 g cm^{-3}, corresponding to the density at the top of the upper mantle and CMB, respectively. The density of MgO slightly increases from 3.51 to 3.61 g cm^{-3} in the upper mantle, and it becomes much more dense as it moves toward the lower mantle. On the other hand, as the mantle moves deeper, the TC of MgO under the 2(mod)+3+4 mechanism continuously decreases from 45.88 to 15.35 $\text{Wm}^{-1} \, \text{K}^{-1}$ in the upper mantle, but it increases to 23.67 $\text{Wm}^{-1} \, \text{K}^{-1}$ at CMB.

[1] E. Ito and E. Takahashi, Postspinel transformations in the system Mg2SiO4-Fe2SiO4 and some geophysical implications, J. Geophys. Res. Solid Earth **94**, 10637 (1989).

[2] K.-J. Chang and M. L. Cohen, High-pressure behavior of MgO: Structural and electronic properties, Phys. Rev. B **30**, 4774 (1984).

[3] M. Mehl, R. Cohen, and H. Krakauer, Linearized augmented plane wave electronic structure calculations for MgO and CaO, J. Geophys. Res. Solid Earth **93**, 8009 (1988).

[4] B. Karki, R. D. Wentzcovitch, S. De Gironcoli, and S. Baroni, First-principles determination of elastic anisotropy and wave velocities of MgO at lower mantle conditions, Science **286**, 1705 (1999).

[5] A. Zerr and R. Boehler, Constraints on the melting temperature of the lower mantle from high-pressure experiments on MgO and magnesioustite, Nature (London) **371**, 506 (1994).

[6] A. M. Hofmeister, Thermal diffusivity and thermal conductivity of single-crystal MgO and Al₂O₃ and related compounds as a function of temperature, Phys. Chem. Miner. **41**, 361 (2014).

[7] D. A. Dalton, W.-P. Hsieh, G. T. Hohensee, D. G. Cahill, and A. F. Goncharov, Effect of mass disorder on the lattice thermal

conductivity of MgO periclase under pressure, Sci. Rep. **3**, 2400 (2013).

[8] G. M. Manthilake, N. de Koker, D. J. Frost, and C. A. McCammon, Lattice thermal conductivity of lower mantle minerals and heat flux from Earth's core, Proc. Natl. Acad. Sci. USA **108**, 17901 (2011).

[9] N. de Koker, Thermal Conductivity of MgO Periclase from Equilibrium First Principles Molecular Dynamics, Phys. Rev. Lett. **103**, 125902 (2009).

[10] S. Stackhouse, L. Stixrude, and B. B. Karki, Thermal Conductivity of Periclase (MgO) from First Principles, Phys. Rev. Lett. **104**, 208501 (2010).

[11] V. Haigis, M. Salanne, and S. Jahn, Thermal conductivity of MgO, MgSiO₃ perovskite and post-perovskite in the Earth's deep mantle, Earth Planet. Sci. Lett. **355**, 102 (2012).

[12] X. Tang and J. Dong, Pressure dependence of harmonic and anharmonic lattice dynamics in MgO: A first-principles calculation and implications for lattice thermal conductivity, Phys. Earth Planet. Inter. **174**, 33 (2009).

[13] X. Tang and J. Dong, Lattice thermal conductivity of MgO at conditions of Earth's interior, Proc. Natl. Acad. Sci. USA **107**, 4539 (2010).

[14] H. Dekura and T. Tsuchiya, Ab initio lattice thermal conductivity of MgO from a complete solution of the linearized Boltzmann transport equation, Phys. Rev. B **95**, 184303 (2017).

[15] M. Puligheddu, Y. Xia, M. Chan, and G. Galli, Computational prediction of lattice thermal conductivity: A comparison of molecular dynamics and Boltzmann transport approaches, Phys. Rev. Materials **3**, 085401 (2019).

[16] N. K. Ravichandran and D. Broido, Non-monotonic pressure dependence of the thermal conductivity of boron arsenide, Nat. Commun. **10**, 1 (2019).

[17] T. Feng and X. Ruan, Quantum mechanical prediction of four-phonon scattering rates and reduced thermal conductivity of solids, Phys. Rev. B **93**, 045202 (2016).

[18] Y. Xia, Revisiting lattice thermal transport in PbTe: The crucial role of quartic anharmonicity, Appl. Phys. Lett. **113**, 073901 (2018).

[19] V. Goldman, G. Horton, and M. Klein, An Improved Self-Consistent Phonon Approximation, Phys. Rev. Lett. **21**, 1527 (1968).

[20] See Supplemental Material at http://link.aps.org/supplemental/10.1103/PhysRevB.102.184309 for details of computations, reliability, and convergence of interatomic force constants.

[21] G. Kresse and D. Joubert, From ultrasoft pseudopotentials to the projector augmented-wave method, Phys. Rev. B **59**, 1758 (1999).

[22] F. Zhou, W. Nielson, Y. Xia, and V. Ozoliņš, Compressive sensing lattice dynamics, I. General formalism, Phys. Rev. B **100**, 184308 (2019).

[23] F. Zhou, B. Sadigh, D. Åberg, Y. Xia, and V. Ozoliņš, Compressive sensing lattice dynamics. II. Efficient phonon calculations and long-range interactions, Phys. Rev. B **100**, 184309 (2019).

[24] S. Baroni and R. Resta, Ab initio calculation of the macroscopic dielectric constant in silicon, Phys. Rev. B **33**, 7017 (1986).

[25] M. Gajdoš, K. Hummer, G. Kresse, J. Furthmüller, and F. Bechstedt, Linear optical properties in the projector-augmented wave methodology, Phys. Rev. B **73**, 045112 (2006).

[26] F. Zhou, W. Nielson, Y. Xia, and V. Ozoliņš, Lattice Anharmonicity and Thermal Conductivity from Compressive Sensing of First-Principles Calculations, Phys. Rev. Lett. **113**, 185501 (2014).

[27] G. P. Srivastava, *The Physics of Phonons* (Routledge, Abingdon, Oxfordshire, England, 2019).

[28] A. Erba, M. Shahrokhi, R. Moradian, and R. Dovesi, On how differently the quasi-harmonic approximation works for two isostructural crystals: Thermal properties of periclase and lime, J. Chem. Phys. **142**, 044114 (2015).

[29] P. Carrier, R. Wentzcovitch, and J. Tsuchiya, First-principles prediction of crystal structures at high temperatures using the quasiharmonic approximation, Phys. Rev. B **76**, 064116 (2007).

[30] H. Clyde and M. L. Klein, Anharmonic effects and the lattice dynamics of insulators, Crit. Rev. Solid State Mater. Sci. **2**, 181 (1971).

[31] I. Errea, B. Rousseau, and A. Bergara, Anharmonic Stabilization of the High-Pressure Simple Cubic Phase of Calcium, Phys. Rev. Lett. **106**, 165501 (2011).

[32] T. Tadano and S. Tsuneyuki, Self-consistent phonon calculations of lattice dynamical properties in cubic SrTiO3 with first-principles anharmonic force constants, Phys. Rev. B **92**, 054301 (2015).

[33] Y. Oba, T. Tadano, R. Akashi, and S. Tsuneyuki, First-principles study of phonon anharmonicity and negative thermal expansion in ScF3, Phys. Rev. Materials **3**, 033601 (2019).

[34] J. M. Ziman, *Electrons and Phonons: The Theory of Transport Phenomena in Solids* (Oxford University Press, Oxford, England, 2001).

[35] T. Feng, L. Lindsay, and X. Ruan, Four-phonon scattering significantly reduces intrinsic thermal conductivity of solids, Phys. Rev. B **96**, 161201(R) (2017).

[36] W. Li, J. Carrete, N. A. Katcho, and N. Mingo, ShengBTE: A solver of the Boltzmann transport equation for phonons, Comput. Phys. Commun. **185**, 1747 (2014).

[37] A. Ward, D. Broido, D. A. Stewart, and G. Deinzer, Ab initio theory of the lattice thermal conductivity in diamond, Phys. Rev. B **80**, 125203 (2009).

[38] P. Carruthers, Resonance in phonon-phonon scattering, Phys. Rev. **125**, 123 (1962).

[39] Y. Xia, K. Pal, J. He, V. Ozoliņš, and C. Wolverton, Particlelike Phonon Propagation Dominates Ultralow Lattice Thermal Conductivity in Crystalline Tl3VSe4, Phys. Rev. Lett. **124**, 065901 (2020).

[40] G. Fiquet, P. Richet, and G. Montagnac, High-temperature thermal expansion of lime, periclase, corundum and spinel, Phys. Chem. Miner. **27**, 103 (1999).

[41] W. Joswig, T. Stachel, J. W. Harris, W. H. Baur, and G. P. Brey, New Ca-silicate inclusions in diamonds—Tracers from the lower mantle, Earth Planet. Sci. Lett. **173**, 1 (1999).

[42] R. Nomura, K. Hirose, K. Uesugi, Y. Ohishi, A. Tsuchiyama, A. Miyake, and Y. Ueno, Low core-mantle boundary temperature inferred from the solidus of pyrolite, Science **343**, 522 (2014).

[43] A. Rao and K. Narender, Studies on thermophysical properties of CaO and MgO by γ-ray attenuation, J. Thermodyn. **2014**, 123478 (2014).

[44] J. Shanker, S. Kushwah, and P. Kumar, Theory of thermal expansivity and bulk modulus for MgO and other minerals at high temperatures, Phys. B: Condens. Matter. **233**, 78 (1997).

[45] M. Sangster, G. Peckham, and D. Saunderson, Lattice dynamics of magnesium oxide, J. Phys. C: Solid State Phys. **3**, 1026 (1970).

[46] S. Ghose, M. Krisch, A. R. Oganov, A. Beraud, A. Bosak, R. Gulve, R. Seelaboyina, H. Yang, and S. K. Saxena, Lattice Dynamics of MgO at High Pressure: Theory and Experiment, Phys. Rev. Lett. **96**, 035507 (2006).

[47] L. Dubrovinsky and S. Saxena, Thermal expansion of periclase (MgO) and tungsten (W) to melting temperatures, Phys. Chem. Miner. **24**, 547 (1997).

[48] Y. Fei, Effects of temperature and composition on the bulk modulus of (Mg, Fe) O, Am. Mineral. **84**, 272 (1999).

[49] A. J. Slifka, B. J. Filla, and J. Phelps, Thermal conductivity of magnesium oxide from absolute, steady-state measurements, J. Res. Natl. Inst. Stand. Technol. **103**, 357 (1998).